Systematic investigation of positron annihilation in transition metals from first principles

Qigui Yang [1,2,3,*] Xingzhong Cao [2] Baoyi Wang [2] Ping Wang [3] and Pär Olsson [1]

[1] *KTH Royal Institute of Technology, Nuclear Engineering, Roslagstullsbacken 21, 114 21 Stockholm, Sweden*

[2] *Institute of High Energy Physics, CAS, Beijing 100049, China*

[3] *China Spallation Neutron Source, Institute of High Energy Physics, CAS, Dongguan 523803, China*

(Received 18 May 2023; revised 18 July 2023; accepted 15 September 2023; published 28 September 2023)

In this work, we present a systematic theoretical study on the positron annihilation characteristics (positron lifetimes and momentum distributions) in transition metals ($3d$, $4d$, and $5d$ metals) and other elements (carbon, aluminum, silicon, and phosphorus). Our calculations agree well with available reference experimental and theoretical data. We show that clear patterns exist in the evolution of the positron annihilation characteristics in pure elements. The evolution of momentum distribution in one transition metal series is mainly contributed by the filling of d-band electrons. For the positron lifetimes, the lifetimes of transition metals evolve with their d-band filling in a similar behavior as their atomic volumes. A case study is performed to show qualitatively the effect of solute elements on the Doppler spectra of defects. It is demonstrated that vacancy-solute complexes depict similar annihilation characteristics as the corresponding pure solute elements, meaning that vacancy-solute complexes can be reliably identified if the Doppler spectra of the pure solute elements are known. For the positron lifetimes, we found that they have a linear relation with the atomic volumes of elements for the same transition metal series. This work is expected to improve understanding of the positron annihilation characteristics of transition metals. The results could be used to investigate and identify the microstructures in alloys and compounds, such as vacancy-solute complexes, solute clusters, precipitates, and vacancies in different sublattices of compounds.

DOI: 10.1103/PhysRevB.108.104113

I. INTRODUCTION

The mechanical properties of metallic materials are significantly affected by solute elements and lattice defects. Different solute elements exist in metallic alloys either as intentionally added alloying elements or as impurities. Many theoretical studies have shown that vacancy-solute complexes are formed because of the attractive interactions between vacancy and solute atoms in lattice [1–3]. The diffusion of these complexes is vital to defect evolution and the formation of solute clusters and nanoprecipitates. These defects and precipitates in materials eventually play important roles in determining the mechanical properties. Therefore, it is crucial to investigate these atomic-scale vacancy-solute complexes in materials. However, due to their small size, these complexes are hard to be directly detected by conventional techniques, such as transmission electron microscopy.

Positron annihilation spectroscopy (PAS) is a nondestructive technique that is sensitive to atomic-scale vacancy-type defects in materials [4]. It has been broadly applied to investigate the lattice and defect properties of metals and semiconductors [4,5]. The two most frequently used PAS methods are positron lifetime spectroscopy and Doppler broadening spectroscopy (DBS) [4]. Positron lifetime measurements are sensitive to defect sizes, which could yield the information about the vacancy cluster sizes in materials [4,6,7], but they are very insensitive to the local chemical environments of defects. DBS is, on the contrary, very sensitive to the local chemical environments of defects. Numerous studies [8–12] have demonstrated that, both in metals and semiconductors, the solute atoms near defects can be clearly seen and distinguished with DBS. Hence, DBS is an important technique for investigating atomic-scale defects in materials.

The Doppler spectra of atomic-scale defects in alloys may depict the characteristic features of the pure elements [13]. For example, various experimental and theoretical studies on alloy systems, such as iron-based alloys [8,14–17] and aluminum-based alloys [10,18–21], have shown that the vacancy-solute atom complexes and solute atom clusters depict similar annihilation characteristics, particularly Doppler spectra, as the corresponding pure solute elements. Therefore, knowing the Doppler spectra of pure elements is one fundamental step to understanding the microstructural evolution of alloy systems. The recent development of the two-component density functional theory (TCDFT) [4,22] provides the opportunity to compute the Doppler spectra of pure elements with satisfactory accuracy. However, while there are both many experimental and theoretical works that contributed the Doppler spectra of various pure elements [13,23–25], no study has yet been carried out to cover the systematics in pure metals. The potential systematics in the transition metal series has not yet been fully revealed or discussed.

In this work, we present the first-principles calculations of transition metals. Other elements (carbon, aluminum, silicon, phsophorus) are also included as they also commonly exist in crystalline materials. We calculated the positron lifetimes and Doppler broadening spectra of these elements with TCDFT.

*Corresponding author: yangqg@ihep.ac.cn

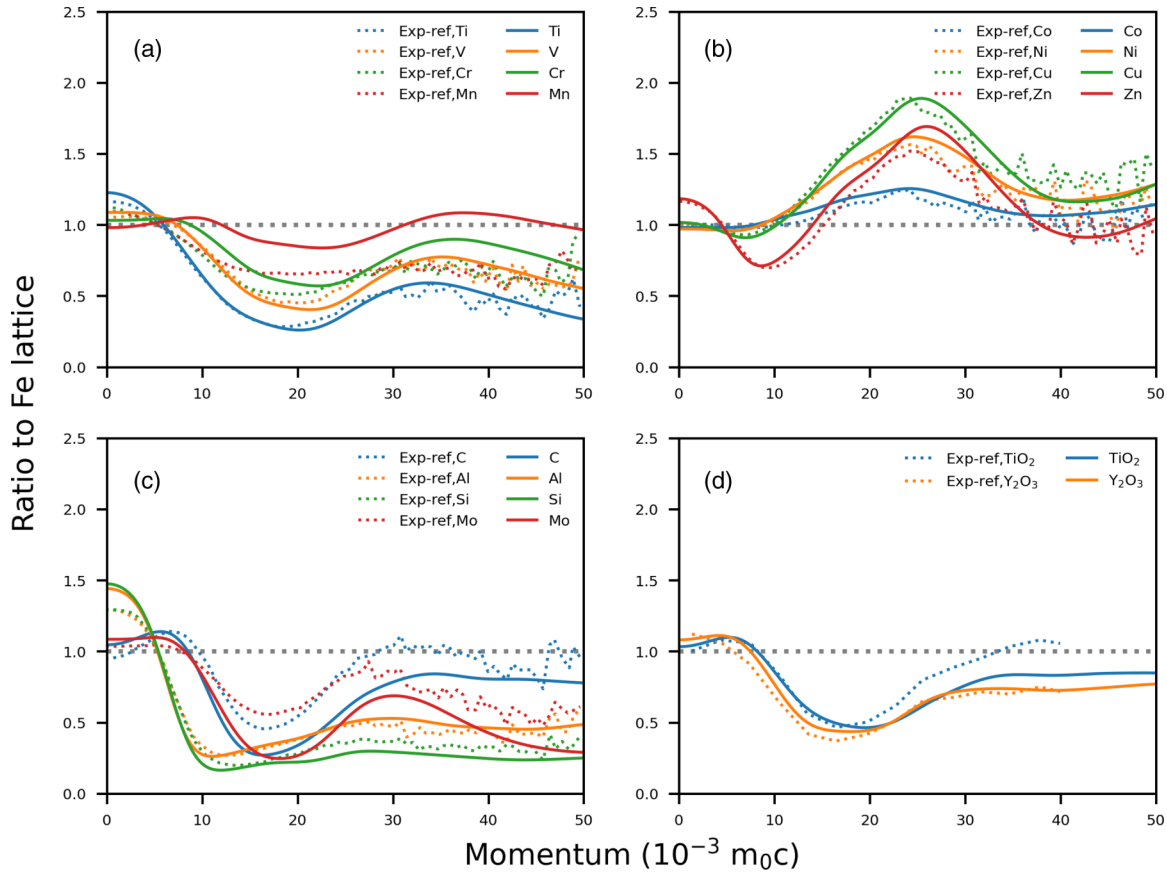

FIG. 1. Doppler spectra of the 3*d* transition metals and other materials. The gray, dashed horizontal lines indicate the bcc iron lattice. The reference experimental data in (a)–(c) are from Ref. [13]. The reference experimental data in (d) are from Ref. [37]. The computational results are convoluted with a Gaussian function with a FWHM of $4.3 \times 10^{-3}\ m_0c$, which corresponds to the experimental resolution.

The calculated results are compared with the available experimental results. The evolution of the Doppler broadening spectra is deeply analyzed by calculating the contributions of each electron shell. We also present a qualitative case study to illustrate the influences of solute atoms on the Doppler spectra of defects. This work is expected to provide a deeper understanding to determine the microstructures in materials by using PAS.

II. COMPUTATIONAL METHODS

The first-principles calculations were performed using the Vienna *ab initio* Simulation Package (VASP) [26] code with the projector augmented-wave (PAW) [27] method. We used the generalized gradient approximation with the Perdew-Burke-Ernzerhof exchange-correlation functional [28] for the electron exchange and correlation potential. The lattice constants of all materials were self-consistently relaxed using DFT. When calculating the lattice constants of graphite carbon and phosphorous, the van der Waals force was included with the generalized gradient approximation-D2 method developed by Grimme *et al.* [29]. The $4 \times 4 \times 4$ conventional bcc supercells with 128 lattice sites were used for the calculations of vacancy-solute complexes. The $3 \times 3 \times 3$ Γ-centered *k*-point mesh was used for these supercells. We tested that these settings yield similar positron annihilation characteristics, with the results calculated by the $6 \times 6 \times 6$ conventional bcc supercells with 432 lattice sites and $2 \times 2 \times 2$ Γ-centered *k*-point mesh. The plane-wave cutoff energy was set to 520 eV for all calculations. The standard potentials from the VASP library were used for all elements. The convergence criterion of ionic relaxation was 0.01 eV/Å.

After the density functional theory (DFT) calculations, we then solved the positron state based on the electronic structures computed by DFT. The implementation to compute the positron density and positron annihilation characteristics was developed by Makkonen *et al.* [22]. We describe the methods of positron modeling; the complete description of the code and theory can be found in Refs. [4,22,30]. In this work, the so-called conventional scheme [4,22] was utilized, in which the positron was approximated not to affect the average electron density, and the zero-positron-density limit was used [31]. This scheme was shown to yield results that agree well with more self-consistent modeling due to certain compensation and feedback effects [32]. In this computational scheme, after the electronic structure was computed by DFT, the positron state can then be solved in the potential as [4,22]

$$V_+ = -\int d\boldsymbol{r}' \frac{n_e(\boldsymbol{r}')}{|\boldsymbol{r}-\boldsymbol{r}'|} - V_{\text{ext}}(\boldsymbol{r}) + V_{\text{corr}}(\boldsymbol{r}), \tag{1}$$

where the V_{ext} is the external potential, n_e is the electron density, and V_{corr} is the zero-density limit of the electron-positron correlation potential $\delta E_c^{e-p}/\delta n_p(\boldsymbol{r})$ [31,33], in which E_c^{e-p} and n_p are electron-positron correlation energy functional and

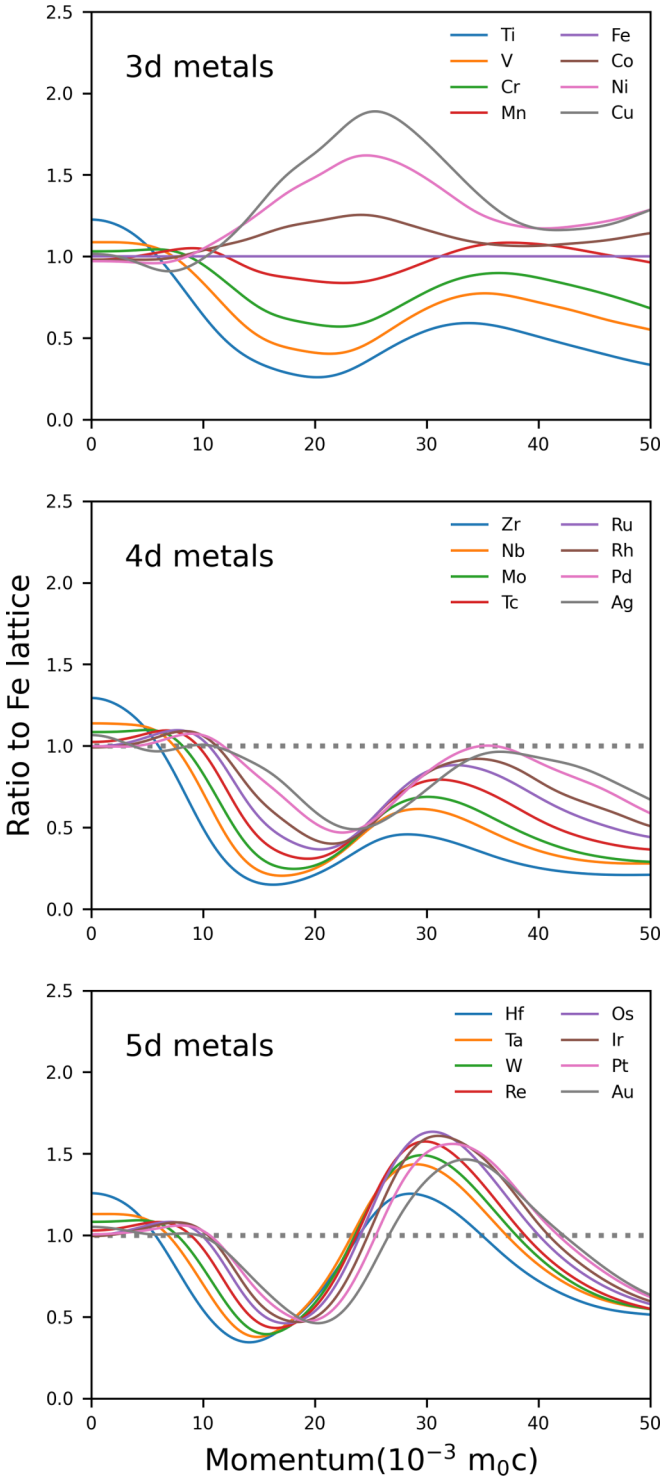

FIG. 2. The calculated Doppler spectra of all transition metals. The gray, dashed horizontal lines indicate the bcc iron lattice. The computational results are convoluted with a Gaussian function with a FWHM of $4.3 \times 10^{-3}\, m_0 c$, which is close to the resolution of typical experimental positron facilities.

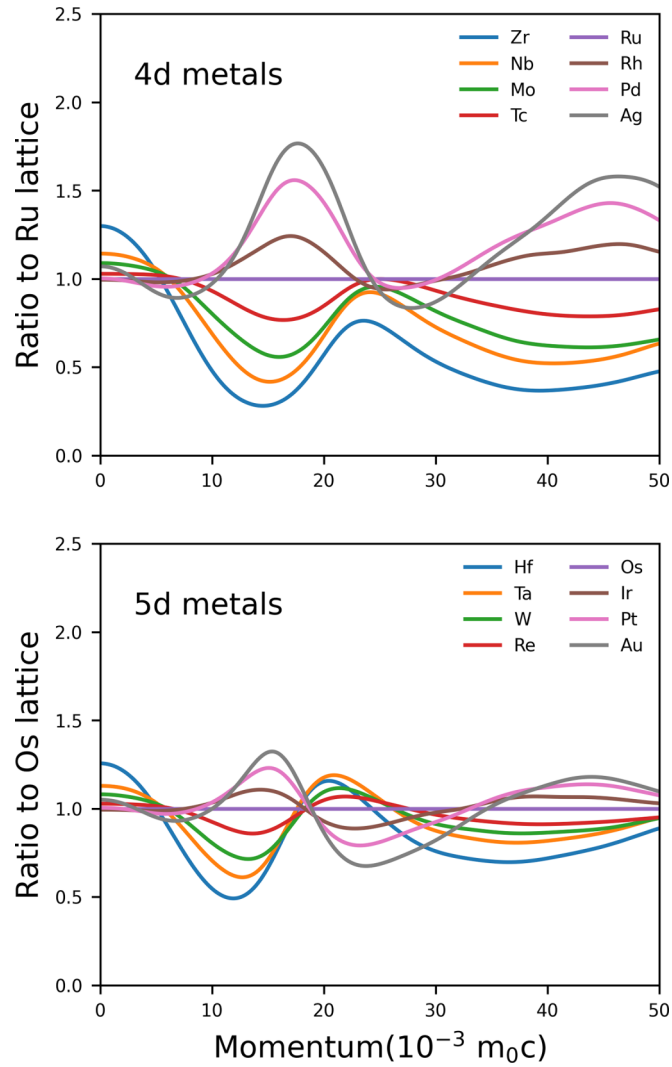

FIG. 3. The calculated Doppler spectra of 4*d* and 5*d* transition metals. Ruthenium and osmium are used as references to present the ratio curves of 4*d* and 5*d* metals, respectively. These two elements are in the same group as iron in periodic table (group 8). The computational results are convoluted with a Gaussian function with a FWHM of $4.3 \times 10^{-3}\, m_0 c$, which is close to the resolution of typical experimental positron facilities.

positron density, respectively. For systems with vacancy-type defects (single vacancy and vacancy-solute complexes), the positron-induced repulsive forces on ions are also included in our calculations. The positron-induced force on ion j is the negative gradient of the lowest positron energy eigenvalue (ε_+) corresponding to the potential of Eq. (1) [4,22]. The positron-induced force F_j^+ is expressed as [4,22]

$$F_j^+ = -\nabla_j \varepsilon_+ = -\langle \psi_p | \nabla_j H(\boldsymbol{r}) | \psi_p \rangle = \int d\boldsymbol{r} n_p(\boldsymbol{r}) [-\nabla_j V_+(\boldsymbol{r})], \quad (2)$$

where ψ_p is the positron wavefunction, $H(\boldsymbol{r})$ is the positron's single-particle Hamiltonian, and $V_+(\boldsymbol{r})$ is approximated with the atomic superposition method [34] as

$$V_+(\boldsymbol{r}) = \sum_j V_{\text{Coul}}^j(|\boldsymbol{r} - \boldsymbol{R}_j|) + V_{\text{corr}}\left(\sum_j n_e^j(|\boldsymbol{r} - \boldsymbol{R}_j|)\right), \quad (3)$$

where V_{Coul}^j is the Coulomb potential and n_e^j is the charge density of ion j. The positron-induced forces would lead to the positron-induced ionic relaxations. Such relaxations

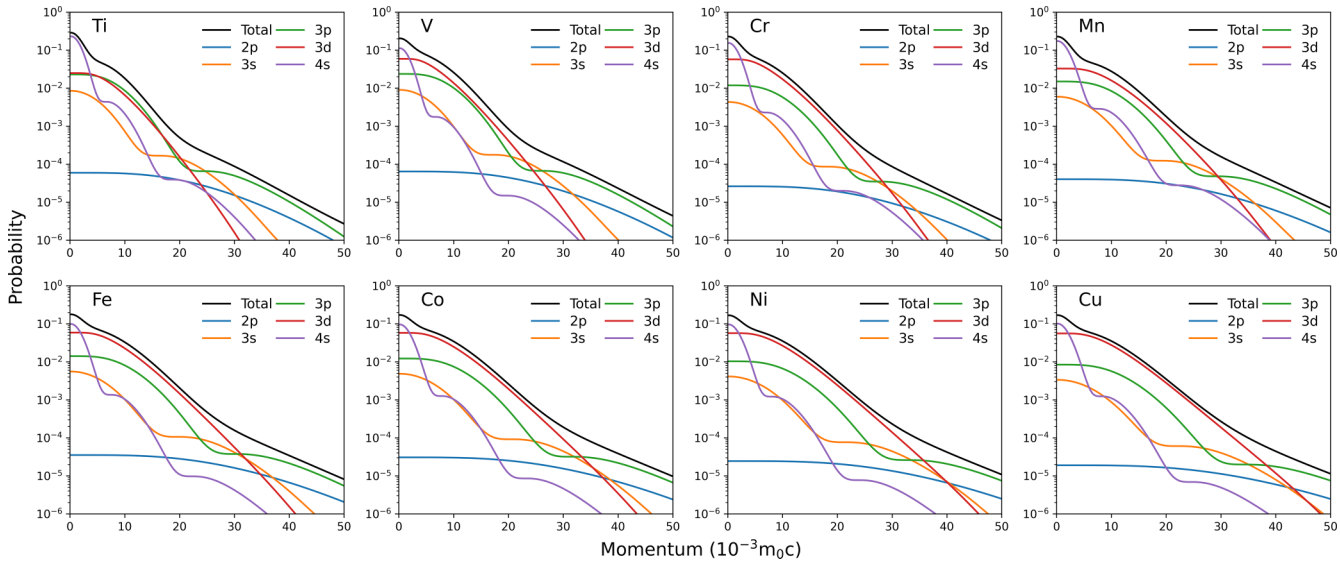

FIG. 4. The contributions of the different electron shells to the positron annihilation in 3*d* metals. The results were calculated using the atomic superposition method [34]. Only the outermost five electron shells are presented, since the contributions of the other electron shells are negligible.

are particularly important to calculate accurately the positron annihilation characteristics in vacancy-type defects. For instance, in this work, for pure iron, the calculated positron lifetimes of single vacancy before and after including the positron-induced forces are 146 ps and 170 ps, respectively. The experimental positron lifetime of single vacancy in iron is ∼175 ps [35]. It is clear that, with the positron-induced forces, the calculated lifetime agrees well with the experimental value. In this work, all supercells with vacancy-type defects were fully relaxed by including the repulsive forces on atoms induced by the localized positron. A more comprehensive comparison on the effect of positron-induced relaxation can be found in Ref. [22].

The positron lifetime τ was calculated as [22]

$$\lambda = \frac{1}{\tau} = \pi r_e^2 c \int d\boldsymbol{r} n_e(\boldsymbol{r}) n_p(\boldsymbol{r}) \gamma(n_e(\boldsymbol{r})), \tag{4}$$

where λ is the annihilation rate, r_e is the classical electron radius, c is the light speed, and $\gamma(n_e(\boldsymbol{r}))$ is the enhancement factor [31]. The momentum distribution $\rho(\boldsymbol{p})$ of the annihilating electron-positron pairs was calculated by the state-dependent model [36] and the PAW method [22]. It is expressed as

$$\rho(\boldsymbol{p}) = \pi r_e^2 c \sum_j \gamma_j \left| \int d\boldsymbol{r} e^{-i\boldsymbol{p}\cdot\boldsymbol{r}} \psi_p(\boldsymbol{r}) \psi_j(\boldsymbol{r}) \right|^2, \tag{5}$$

TABLE I. Positron lifetimes of transition metals and other elements. Our calculations are compared with theoretical and experimental references.

Element	Calculation (ps)	Experiment[a] (ps)	Element	Calculation (ps)	Experiment[a] (ps)
C (graphite)	184	170, 215	Nb	122, 126[b]	127, 119, 122
C (diamond)	93, 93[b]		Mo	106, 109[b]	119, 103, 121
Al	163, 168[b]	160	Tc	98, 98[b]	
Si	213, 218[b]	220, 228	Ru	94, 94[b]	
P (black)	208		Rh	97, 97[b]	
P (white)	252		Pd	110, 107[b]	98[b]
Ti	142, 147[b]	145, 147, 148	Ag	129, 125[b]	135, 131, 138
V	111, 116[b]	123, 130, 125	Hf	147, 150[b]	179
Cr	96, 104[b]		Ta	117, 119[b]	120[b]
Mn	91, 104[c], 106[b]	121	W	101, 102[b]	115, 105, 120
Fe	96, 102[b]	110, 106, 107	Re	94, 94[b]	
Co	93, 97[b]	100, 119	Os	89, 89[b]	
Ni	95, 96[b]	105, 110	Ir	91, 90[b]	
Cu	106, 108[b]	115, 110, 122	Pt	100, 99[b]	99, 117
Zr	159, 160[b]	159, 165	Au	118, 112[b]	119,117,118

[a]Experimental results are from Ref. [25] and references therein unless specifically marked.
[b]Reference [40].
[c]Calculated in this work with the experimental lattice constant.

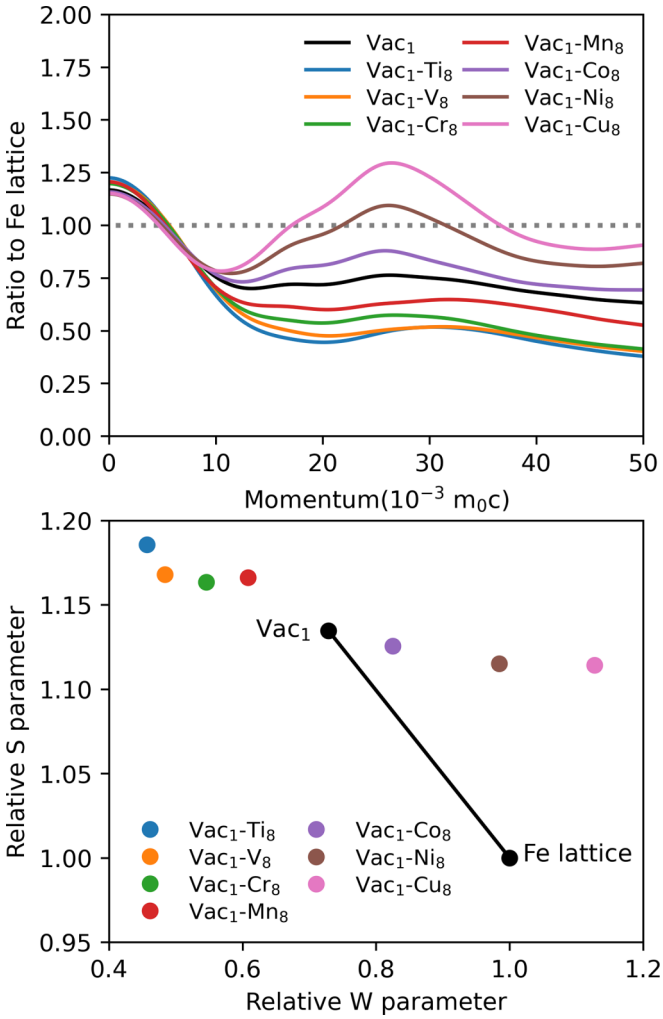

FIG. 5. Top: The Doppler spectra of Vac_1-X_8 complexes (X = 3d metals). The gray, dashed horizontal line indicates the bcc iron lattice. Bottom: The *SW* plot of corresponding complexes. The computational results are convoluted with a Gaussian function with a FWHM of $4.3 \times 10^{-3}\, m_0c$, which is close to the resolution of typical experimental positron facilities.

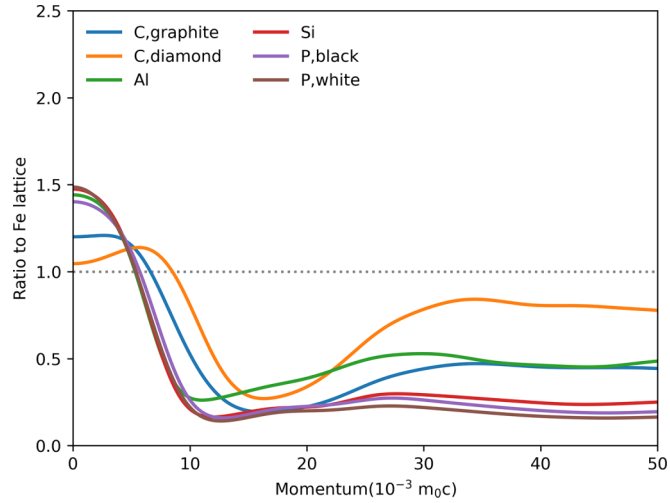

FIG. 6. The Doppler spectra of carbon, aluminum, silicon, and phosphorus. The gray, dashed horizontal line indicates the bcc iron lattice. The computational results are convoluted with a Gaussian function with a FWHM of $4.3 \times 10^{-3}\, m_0c$, which is close to the resolution of typical experimental positron facilities.

where $\psi_j(\boldsymbol{r})$ is the wavefunction of the electron on orbital j, and $\gamma_j = \lambda_j/\lambda_j^{\mathrm{IPM}}$, where λ_j is the annihilation rate of the electron on orbital j. This was calculated in the same way as in Eq. (4). λ_j^{IPM} is the annihilation rate calculated using the independent-particle model (IPM), in which $\gamma \equiv 1$. In this work, the Boroński-Nieminen local density approximation [31] was used for the electron-positron correlation and the enhancement factor. The computed momentum distributions were convoluted with a Gaussian function with a full width at half maximum (FWHM) corresponding to the experimental resolution.

III. RESULTS AND DISCUSSION

A. Doppler broadening spectra

The computed Doppler spectra are presented as the ratio-curve normalized to the momentum distribution of the reference material. In this work, the bcc iron lattice is the main reference material. Figure 1 shows the comparison between the calculated and reference experimental ratio curves of various materials. Figure 1(a)–1(c) presents the curves of transition metals and other solute elements (carbon, aluminum, silicon). Most of the calculated results show excellent agreement with the experimental results. For manganese, the agreement between the calculation and the experiment is less satisfactory, as the calculation overestimates the intensity of the curve. For carbon and molybdenum, the shapes of the calculated curves are similar to the experimental curves, and the agreement at the low-momentum range ($<10 \times 10^{-3}\, m_0c$) is also very good. But, the calculation underestimates the intensity of the curve at a higher momentum range ($>10 \times 10^{-3}\, m_0c$). Figure 1(d) presents the curves of TiO_2 and Y_2O_3. These two oxides are included as they are widely used in oxide dispersion-strengthened alloys. The curve of Y_2O_3 is in very good agreement with the experimental data. For TiO_2, our calculation agrees well with the experimental result at a low momentum, and it shows a slight underestimation of intensity at a higher momentum.

Figure 1 shows that TCDFT can generally yield reasonable results for different materials. Therefore, we present a systematic comparison of the Doppler broadening spectra of transition metals (3d, 4d, and 5d) in Fig. 2. Clear patterns are shown in all transition metal series. For the 3d metals, there are broad valleys/peaks at $\sim 20 \times 10^{-3}\, m_0c$. The intensities of the valleys/peaks increase with the d-band filling of elements. These characteristics are useful to detect and distinguish vacancy-solute complexes or solute clusters in alloys. For instance, many studies have shown that PAS can detect copper clusters in an iron matrix with or without the existence of vacancies [8,15,16,38,39]. Therefore, it is also expected that other 3d metal solutes in iron are detectable and even distinguishable by PAS if vacancy-solute complexes or solute clusters are formed. For 4d and 5d metals, their spectra also have valleys and peaks at ~ 15 to $20 \times 10^{-3}\, m_0c$

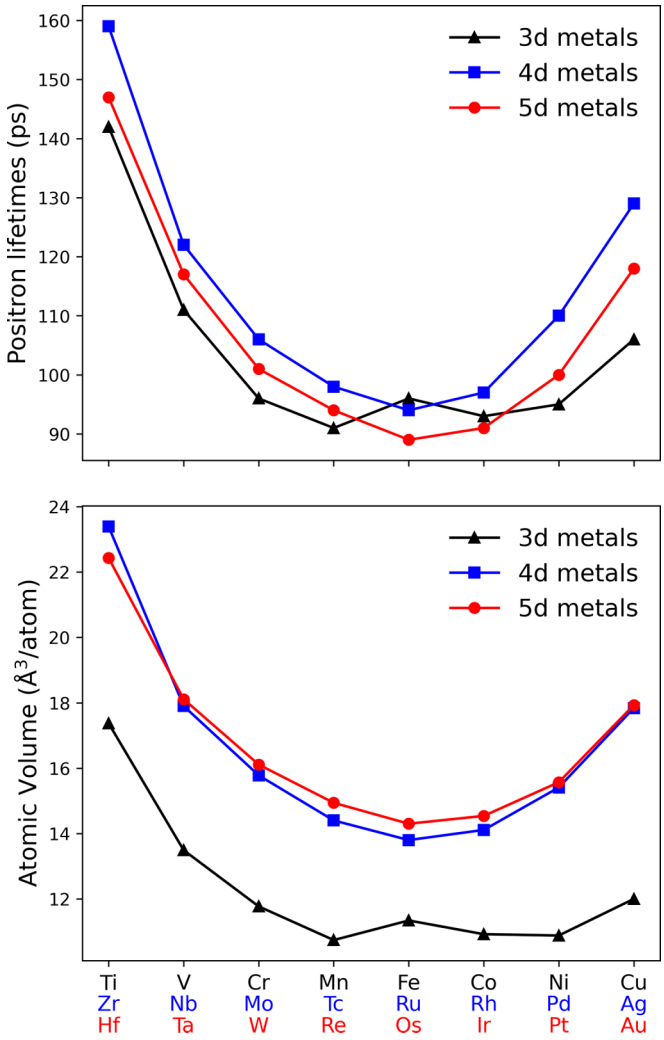

FIG. 7. Top: Positron lifetime as a function of d-band filling. Bottom: Atomic volume as a function of d-band filling.

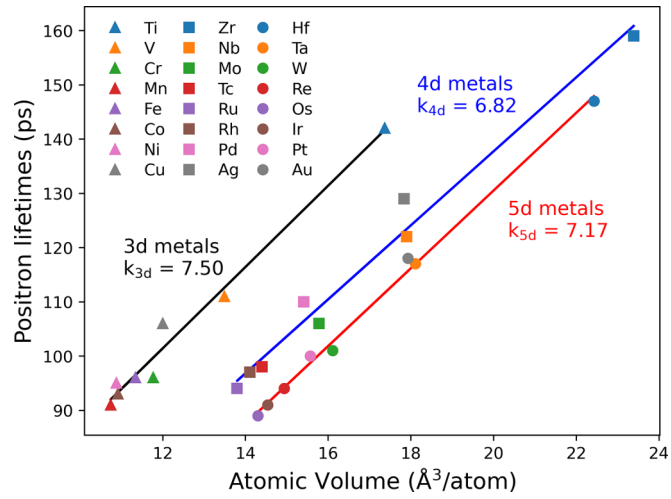

FIG. 8. The positron lifetime as a function of atomic volume. The linear regressions of each metal series are included. k_i ($i = 3d, 4d, 5d$) is the slope of each line.

and at $\sim 30 \times 10^{-3}\, m_0 c$, respectively. Figure 2 shows that the characteristic valleys and peaks of $4d$ and $5d$ metals are not as unique as $3d$ metals. This seems to imply that the detectability and distinguishability of $4d$ and $5d$ metals in alloys is not as good as $3d$ metals. However, the choice of the reference material is also decisive. Figure 3 presents the ratio curves of $4d$ and $5d$ metals using ruthenium and osmium as references, respectively. These two reference elements are in the same column as iron in periodic table. It is shown that, using different reference elements, the trends in the $4d$ and $5d$ series are similar to those of the $3d$ series. This indicates that the $4d$ and $5d$ elements are also distinguishable from each other with the proper choice of reference materials.

We have shown in Figs. 2 and 3 that clear patterns exist in the Doppler spectra of transition metals. This is mainly contributed by the filling of d-band electrons. Figure 4 shows the calculated contributions of electron shells involved in the positron annihilation in $3d$ metals. It is clear that at the momentum range between ~ 5 and $\sim 30 \times 10^{-3}\, m_0 c$, the contribution of the $3d$ electrons gradually increases with the d-band filling. For titanium, both $3p$- and $3d$-electrons dominate at the momentum range between ~ 5 and $\sim 30 \times 10^{-3}\, m_0 c$, and the $3p$-electrons dominate at a higher momentum ($> 30 \times 10^{-3}\, m_0 c$). For copper, the contribution of the $3d$-electrons is much higher than the other electron shells, and the $3d$-electrons dominate at the momentum range between ~ 5 and $\sim 40 \times 10^{-3}\, m_0 c$. The increase of the contribution of $3d$-electrons results in an increase in the intensities of the valleys/peaks of $3d$ metals in Fig. 2. For $4d$ and $5d$ metals, the evolution of their Doppler spectra also changes with the filling of d-band electrons. The details of the contribution of electron shells for $4d$ and $5d$ metals are included in the Appendix.

We also present a simple qualitative case study on $3d$ metals since they are frequent alloying elements in ferritic alloys, which is one of the most widely used alloy types. Solute clustering, either induced by thermal treatment or radiation, is a common phenomenon in ferritic alloys. Vacancies can bind with solute atoms and form Vac-X_n ($X = 3d$ metals, $n \geqslant 1$) complexes [1,3]. In crystalline materials, the Doppler broadening spectra of vacancies would then be influenced by the neighboring solute atoms, as clearly shown in various theoretical and experimental works [8,15,16,19]. Such information might be used to identify the type of solute atoms near vacancies. In the bcc structure, each atom has eight first nearest neighbors (1NNs). In this qualitative case study, we enforced one single vacancy to bind with eight $3d$ metal atoms at 1NN positions and form Vac_1-X_8 complexes. We emphasize that we understand such cases are probably not realistic for elements like titanium or vanadium, but it is possible to happen for elements with a strong clustering tendency, such as copper. The purpose of this case study is to understand qualitatively the effect of solute atoms on the Doppler spectra of vacancy defects. Figure 5 shows the Doppler spectra and SW plot of Vac_1-X_8 complexes. The Doppler spectra show a similar trend as that seen in Fig. 2 for pure $3d$ metals. At a low momentum, the difference between the complexes is small; at a higher momentum (~ 20 to $25 \times 10^{-3}\, m_0 c$), the intensities of curves gradually increase with d-band filling. Broad peaks at a high momentum are observed for cobalt, nickel, and

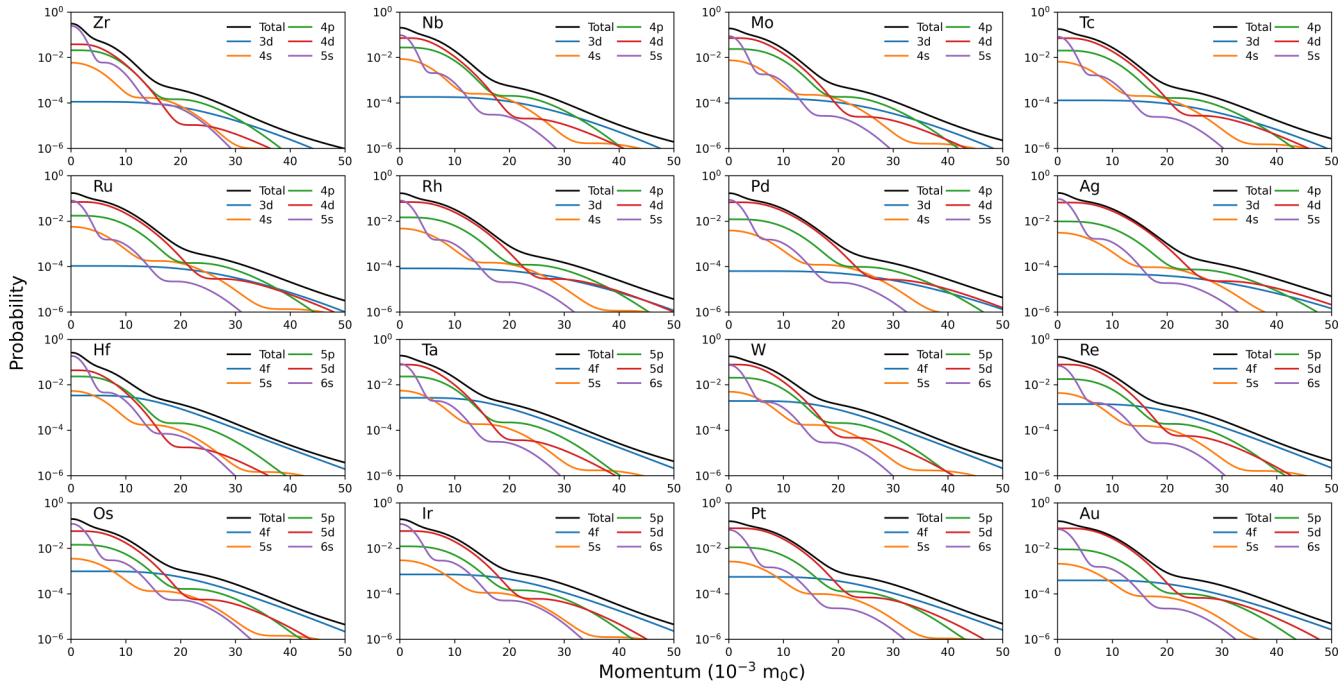

FIG. 9. The contributions of the electron shells in the positron annihilation in 4*d* and 5*d* metals. The results were calculated using the atomic superposition method [34]. Only the outermost five electron shells are presented, since the contributions of the other electron shells are negligible.

copper. The differences in the ratio curves are reflected in the *SW* plot in Fig. 5. In this work, the momentum ranges to calculate the *S* and *W* parameters are 0 to $4 \times 10^{-3}\, m_0c$ and 18 to $30 \times 10^{-3}\, m_0c$, respectively. In Fig. 5, both the ratio curves and the *SW* plot clearly illustrate the detectability and distinguishability of 3*d* metals in an iron matrix. For elements with Doppler spectra that are significantly different from iron, such as titanium, vanadium, nickel, and copper, their complexes are easier to be detected and distinguished by Doppler spectra. This is particular for copper, as shown by numerous experimental and theoretical studies [8,15,38,39].

We also calculated the Doppler spectra of other elements, including carbon, aluminum, silicon, and phosphorus, given that they also frequently exist in crystalline materials. For carbon, we used two different structures—graphite and diamond—to calculate the Doppler structure. For phosphorus, we used two different structures—black phosphorus and white phosphorous—to calculate the Doppler spectra. The results are presented in Fig. 6. For carbon, the curves of the graphite and diamond structures are different from each other, while the curves of the black and white phosphorous are similar to each other. This difference between carbon and phosphorous is probably because of the bonding between atoms. In both black and white phosphorous, covalent bonds and van der Waals forces both play important roles in the bonding of atoms. Nevertheless, while the van der Waals forces are important in graphite carbon to bond atom layers, it is negligible in diamond carbon. Figure 6 shows the low-momentum part ($<10 \times 10^{-3}\, m_0c$) of aluminum, silicon, and phosphorus is very similar to each other, but a clear trend exists at the high-momentum part ($>10 \times 10^{-3}\, m_0c$), in which the intensities of curves decrease with the atomic number. The details of the contribution of the electron shells are included in the Appendix.

B. Positron lifetimes

Apart from the Doppler spectra, we also calculated positron lifetimes of pure elements. The calculated positron lifetimes are listed in Table I. They are compared with available reference data. Our calculations agree well with the reference theoretical data of Robles *et al.* [40], in which they also used Boroński-Nieminen parameterization [31]. The difference between our results is considered mainly to be due to the lattice constants used in our work. In this work, all lattice constants were self-consistently relaxed, whereas the experimental lattice constants were used to calculate the positron lifetimes of elements in Ref. [40]. The positron lifetime is very sensitive to the lattice constants of materials. For example, our calculated positron lifetime of manganese is 91 ps with a self-consistent lattice constant ($a = 8.54$ Å) and 104 ps with an experimental lattice constant ($a = 8.91$ Å). In Ref. [40], the positron lifetime of manganese is 106 ps with the experimental lattice constant, which is very close to our calculation (104 ps). Hence, we conclude that the difference between this work and Ref. [40] is mainly due to the different lattice constants. Compared with the experimental positron lifetimes, although our calculations tend to underestimate the positron lifetimes, they still show overall good agreement with the experimental results. This indicates that our calculations not only give good Doppler spectra, but also accurate positron lifetimes.

Figure 7 shows the positron lifetimes and atomic volumes versus d-band filling. For the $4d$ and $5d$ metal series, both the positron lifetimes and atomic volumes demonstrate a U-shaped behavior. They would first decrease, then increase with d-band filling. For the $3d$ metal series, iron is the exception in both the positron lifetimes and atomic volumes. This finally results in the W-shaped behavior of $3d$ metals. For all transition metals, their positron lifetimes evolve with their d-band filling in a behavior similar to their atomic volumes. Such similarity indicates that, for the same transition metal series, the atomic volume is the dominating factor of positron lifetimes. Figure 8 shows the positron lifetime as a function of atomic volume. The positron lifetimes of transition metals clearly show a linear relation with the atomic volumes of elements. The linear regressions of each metal series are presented to show the trends. The slopes of each fitted straight line are very close to each other. Figure 8 indicates that, for each transition metal series, their lattice positron lifetimes could be easily estimated, with reasonable accuracy, with the atomic volume using a simple linear equation.

IV. CONCLUSION

We have presented a systematic study of positron annihilation in transition metals and other elements (carbon, aluminum, silicon, and phosphorus). The state-of-the-art TCDFT is used to reveal the systematics of positron annihilation in materials. Our calculations of both Doppler broadening spectra and positron lifetimes agree well with available experimental results. For Doppler broadening spectra, we demonstrate that clear patterns exist in all transition metal series with d-band filling. For the same transition metal series, the evolution of the spectra is mainly contributed by the filling of d-band electrons. A simple qualitative case study is also presented to discuss the detectability of transition metal solutes in an iron matrix. We show that the Doppler spectra of vacancy-solute complexes have similar characteristics as the Doppler spectra of the corresponding solute elements. This case study indicates that the vacancy-solute complexes in materials could be reliably identified if the Doppler spectra of the pure solute elements are known. For positron lifetimes, the calculated positron lifetimes could be used as reference to determine accurately the positron lifetimes of pure metal lattices. Moreover, the lifetimes of transition metals evolve with their d-band filling in a behavior similar to their atomic volumes. For the $4d$ and $5d$ metal series, both lifetimes and atomic volumes first decrease and then increase with their d-band filling. A U-shaped behavior is noted. For $3d$ metals, a W-shaped behavior is seen, as iron is an exception. For the same transition metal series, a linear relation is clearly shown between positron lifetimes and atomic volumes. The results in this work could be used to investigate and identify microstructures in alloys and compounds, such as vacancy-solute complexes, solute atom clusters, and probably vacancies in different sublattices of compounds.

ACKNOWLEDGMENTS

The financial support from the National Key R&D Project (Grant No. 2019YFA0210002) is acknowledged. Q.Y. acknowledges the financial support of the China Scholarship Council (Grant No. 201807930008) and Svensk Karnbranslehantering AB. The funding from the Euratom Research and Training Programme 20192020 (Grant Agreement No. 900018) (EN-TENTE project) is acknowledged. The views and opinions expressed herein do not necessarily reflect those of the European Union or the European Commission. Neither the European Union nor the European Commission can be held responsible for them. The computational resources were provided by the Swedish National Infrastructure for Computing and by the CINECA HPC Center in Italy. The authors gratefully thank Dr. Ilja Makkonen at the University of Helsinki for providing access to the positron code and for many fruitful discussions. The authors gratefully thank Prof. Filip Tuomisto at the University of Helsinki and Dr. Zhiwei Hu at CNRS for generously sharing their insights in PAS.

APPENDIX: DECOMPOSITION OF THE DOPPLER SPECTRA OF ALL OTHER ELEMENTS

Figure 9 shows the contributions of electron shells involved in the positron annihilation in $4d$ and $5d$ metals. In both series, the contributions of d-band ($4d$ or $5d$) electrons at the momentum range between $\sim$5 and $\sim 20 \times 10^{-3}\, m_0 c$ gradually increase with d-band filling and finally dominate the positron annihilation at this momentum range. Such evolution of the contribution of d-band electrons is similar to $3d$ metals, and it is the main reason for the patterns shown in Figs. 2 and 3 for $4d$ and $5d$ metals. At a higher momentum ($>20 \times 10^{-3}\, m_0 c$), for $4d$ metals, both the $3d$- and $4p$-electrons dominate the positron annihilation at this momentum range; for $5d$ metals, both $4f$- and $5p$- electrons dominate the positron annihilation at this momentum range. With d-band filling, the contributions of the $4d$ and $5d$ electrons also gradually increase at the high-momentum range ($>20 \times 10^{-3}\, m_0 c$). This is also similar in $3d$ metals.

Figure 10 shows the contributions of electron shells involved in the positron annihilation in carbon, aluminum, silicon, and phosphorus. For diamond carbon, the contribution of the $1s$-electrons at a high momentum is higher than that of graphite carbon, explaining the higher intensity of diamond carbon at a high momentum in Fig. 6. For aluminum, silicon, and phosphorus, the contribution of the $3p$-electrons increases with the atomic number at a high-momentum range. However, the contribution of $2p$-electrons decreases with the atomic number. The increasing contribution of $3p$-electrons does not fully compensate the decreasing contribution of $2p$-electrons. This finally results in the decreasing intensities with atomic number at a high-momentum range, as shown in Fig. 6.

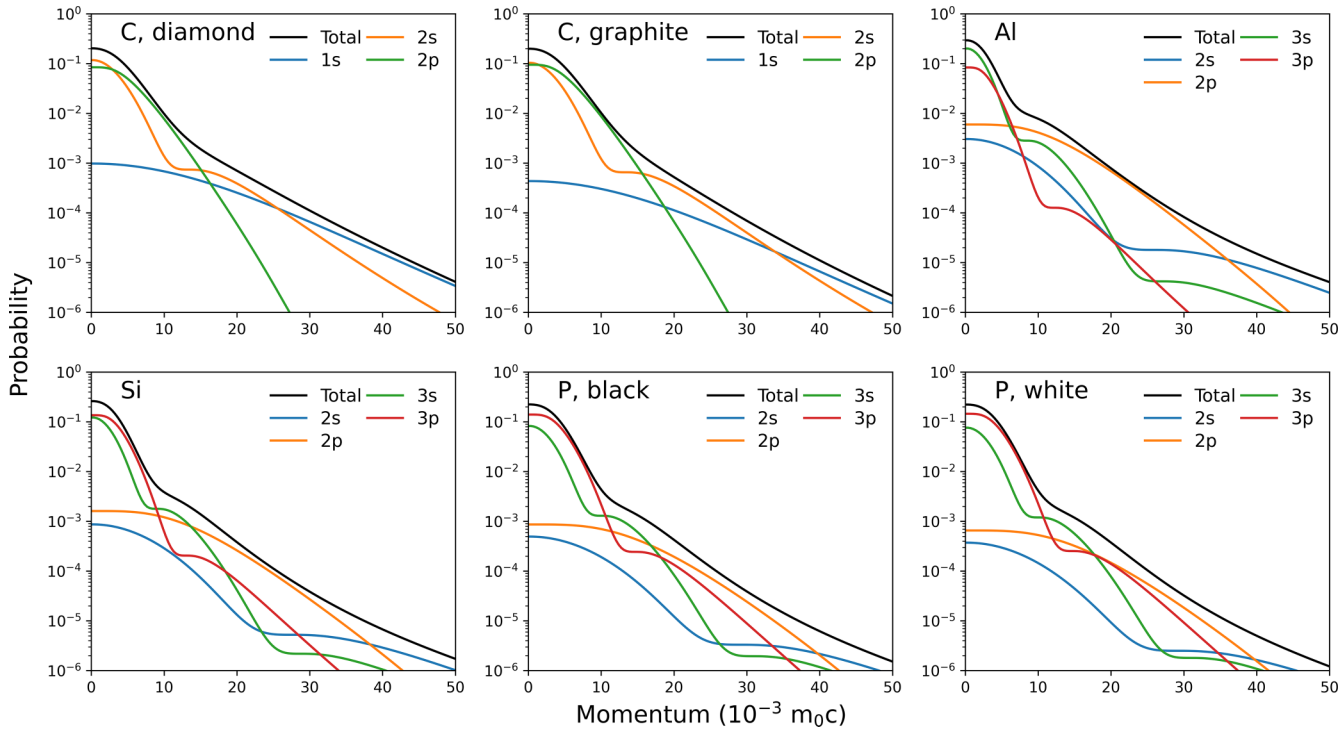

FIG. 10. The contributions of the electron shells in the positron annihilation in carbon, aluminum, silicon, and phosphorus. The results were calculated using the atomic superposition method [34]. For aluminum, silicon, and phosphorus, the 1*s*-electrons are not shown since their contributions are negligible.

[1] A. Claisse and P. Olsson, First-principles calculations of (Y, Ti, O) cluster formation in body centred cubic iron-chromium, Nucl. Instrum. Methods Phys. Res. B **303**, 18 (2013).

[2] L. Messina, M. Nastar, T. Garnier, C. Domain, and P. Olsson, Exact *ab initio* transport coefficients in bcc Fe−*X* (*X* = Cr, Cu, Mn, Ni, P, Si) dilute alloys, Phys. Rev. B **90**, 104203 (2014).

[3] L. Messina, M. Nastar, N. Sandberg, and P. Olsson, Systematic electronic-structure investigation of substitutional impurity diffusion and flux coupling in bcc iron, Phys. Rev. B **93**, 184302 (2016).

[4] F. Tuomisto and I. Makkonen, Defect identification in semiconductors with positron annihilation: Experiment and theory, Rev. Mod. Phys. **85**, 1583 (2013).

[5] J. Čížek, Characterization of lattice defects in metallic materials by positron annihilation spectroscopy: A review, J. Mater. Sci. Technol. **34**, 577 (2018).

[6] Q. Yang, Z. Hu, I. Makkonen, P. Desgardin, W. Egger, M. Barthe, and P. Olsson, A combined experimental and theoretical study of small and large vacancy clusters in tungsten, J. Nucl. Mater. **571**, 154019 (2022).

[7] M. Zibrov, W. Egger, J. Heikinheimo, M. Mayer, and F. Tuomisto, Vacancy cluster growth and thermal recovery in hydrogen-irradiated tungsten, J. Nucl. Mater. **531**, 152017 (2020).

[8] Q. Yang and P. Olsson, Identification and evolution of ultrafine precipitates in Fe-Cu alloys by first-principles modeling of positron annihilation, Acta Mater. **242**, 118429 (2023).

[9] M. Elsayed, T. E. M. Staab, J. Čížek, and R. Krause-Rehberg, Monovacancy-hydrogen interaction in pure aluminum: Experimental and *ab-initio* theoretical positron annihilation study, Acta Mater. **248**, 118770 (2023).

[10] M. Elsayed, T. E. M. Staab, J. Čížek, and R. Krause-Rehberg, On the interaction of solute atoms with vacancies in diluted Al-alloys: A paradigmatic experimental and *ab-initio* study on indium and tin, Acta Mater. **219**, 117228 (2021).

[11] C. Rauch, I. Makkonen, and F. Tuomisto, Identifying vacancy complexes in compound semiconductors with positron annihilation spectroscopy: A case study of InN, Phys. Rev. B **84**, 125201 (2011).

[12] J.- M. Mäki, I. Makkonen, F. Tuomisto, A. Karjalainen, S. Suihkonen, J. Räisänen, T. Y. Chemekova, and Y. N. Makarov, Identification of the V_{Al}-O_N defect complex in AlN single crystals, Phys. Rev. B **84**, 081204(R) (2011).

[13] Y. Nagai, Z. Tang, and M. Hasegawa, Chemical analysis of precipitates in metallic alloys using coincidence Doppler broadening of positron annihilation radiation, Radiat. Phys. Chem. **58**, 737 (2000).

[14] Y. Nagai, M. Hasegawa, Z. Tang, A. Hempel, K. Yubuta, T. Shimamura, Y. Kawazoe, A. Kawai, and F. Kano, Positron confinement in ultrafine embedded particles: Quantum-dot-like state in an Fe-Cu alloy, Phys. Rev. B **61**, 6574 (2000).

[15] Y. Nagai, K. Takadate, Z. Tang, H. Ohkubo, H. Sunaga, H. Takizawa, and M. Hasegawa, Positron annihilation study of

vacancy-solute complex evolution in Fe-based alloys, Phys. Rev. B **67**, 224202 (2003).

[16] T. Toyama, Z. Tang, K. Inoue, T. Chiba, T. Ohkubo, K. Hono, Y. Nagai, and M. Hasegawa, Size estimation of embedded Cu nanoprecipitates in Fe by using affinitively trapped positrons, Phys. Rev. B **86**, 104106 (2012).

[17] J. Čížek, F. Lukáč, O. Melikhova, I. Procházka, and R. Kužel, Thermal vacancies in Fe_3Al studied by positron annihilation, Acta Mater. **59**, 4068 (2011).

[18] X. Liu, P. Zhang, B. Wang, X. Cao, S. Jin, and R. Yu, Study of interaction mechanism between positrons and Ag clusters in dilute Al–Ag alloys at low temperature, Materials **14**, 1451 (2021).

[19] P. Folegati, I. Makkonen, R. Ferragut, and M. J. Puska, Analysis of electron-positron momentum spectra of metallic alloys as supported by first-principles calculations, Phys. Rev. B **75**, 054201 (2007).

[20] M. Elsayed, A. M. Ibrahim, T. E. M. Staab, and R. Krause-Rehberg, A new perspective on the precipitation sequence in a high-purity Al-1.74 at.% Cu alloy by employing positron annihilation spectroscopy: Experiment and theory, J. Phys.: Condens. Matter **33**, 435401 (2021).

[21] J. Banhart, M. Liu, Y. Yong, Z. Liang, C. S. T. Chang, M. Elsayed, and M. D. H. Lay, Study of ageing in Al–Mg–Si alloys by positron annihilation spectroscopy, Phys. B Condens. Matter **407**, 2689 (2012).

[22] I. Makkonen, M. Hakala, and M. J. Puska, Modeling the momentum distributions of annihilating electron-positron pairs in solids, Phys. Rev. B **73**, 035103 (2006).

[23] P. Asoka-Kumar, M. Alatalo, V. J. Ghosh, A. C. Kruseman, B. Nielsen, and K. G. Lynn, Increased Elemental Specificity of Positron Annihilation Spectra, Phys. Rev. Lett. **77**, 2097 (1996).

[24] V. J. Ghosh, M. Alatalo, P. Asoka-Kumar, B. Nielsen, K. G. Lynn, A. C. Kruseman, and P. E. Mijnarends, Calculation of the Doppler broadening of the electron-positron annihilation radiation in defect-free bulk materials, Phys. Rev. B **61**, 10092 (2000).

[25] R. S. Brusa, W. Deng, G. P. Karwasz, and A. Zecca, Doppler-broadening measurements of positron annihilation with high-momentum electrons in pure elements, Nucl. Instrum. Methods Phys. Res. B **194**, 519 (2002).

[26] G. Kresse and J. Furthmüller, Efficient iterative schemes for *ab initio* total-energy calculations using a plane-wave basis set, Phys. Rev. B **54**, 11169 (1996).

[27] P. E. Blöchl, Projector augmented-wave method, Phys. Rev. B **50**, 17953 (1994).

[28] J. P. Perdew, K. Burke, and M. Ernzerhof, Generalized Gradient Approximation Made Simple, Phys. Rev. Lett. **77**, 3865 (1996).

[29] S. Grimme, Semiempirical GGA-type density functional constructed with a long-range dispersion correction, J. Comput. Chem. **27**, 1787 (2006).

[30] I. Makkonen, *Modeling Momentum Distributions of Positron Annihilation Radiation in Solids* (Helsinki University of Technology, Helsinki, 2007).

[31] E. Boroński and R. M. Nieminen, Electron-positron density-functional theory, Phys. Rev. B **34**, 3820 (1986).

[32] M. J. Puska, A. P. Seitsonen, and R. M. Nieminen, Electron-positron Car-Parrinello methods: Self-consistent treatment of charge densities and ionic relaxations, Phys. Rev. B **52**, 10947 (1995).

[33] J. Arponen and E. Pajanne, Electron liquid in collective description: III. Positron annihilation, Ann. Phys. (N Y) **121**, 343 (1979).

[34] M. J. Puska and R. M. Nieminen, Defect spectroscopy with positrons: A general calculational method, J. Phys. F Met. Phys. **13**, 333 (1983).

[35] H. E. Schaefer, Investigation of thermal equilibrium vacancies in metals by positron annihilation, Phys. Status Solidi **102**, 47 (1987).

[36] M. Alatalo, B. Barbiellini, M. Hakala, H. Kauppinen, T. Korhonen, M. J. Puska, K. Saarinen, P. Hautojärvi, and R. M. Nieminen, Theoretical and experimental study of positron annihilation with core electrons in solids, Phys. Rev. B **54**, 2397 (1996).

[37] M. J. Alinger, S. C. Glade, B. D. Wirth, G. R. Odette, T. Toyama, Y. Nagai, and M. Hasegawa, Positron annihilation characterization of nanostructured ferritic alloys, Mater. Sci. Eng. A **518**, 150 (2009).

[38] Y. Nagai, Z. Tang, M. Hassegawa, T. Kanai, and M. Saneyasu, Irradiation-induced Cu aggregations in Fe: An origin of embrittlement of reactor pressure vessel steels, Phys. Rev. B **63**, 134110 (2001).

[39] S. Jin, P. Zhang, E. Lu, L. Guo, B. Wang, and X. Cao, Correlation between Cu precipitates and irradiation defects in Fe–Cu model alloys investigated by positron annihilation spectroscopy, Acta Mater. **103**, 658 (2016).

[40] J. M. C. Robles, E. Ogando, and F. Plazaola, Positron lifetime calculation for the elements of the periodic table, J. Phys.: Condens. Matter **19**, 176222 (2007).